

STRUCTURAL HEALTH MONITORING BY PIEZO-IMPEDANCE

TRANSDUCERS. II: APPLICATIONS

(AS/2003/022179)

Suresh BHALLA¹ and Chee Kiong SOH²

ABSTRACT

This paper, the second in a two-part series, presents a new methodology for structural identification and non-destructive evaluation by piezo-impedance transducers. The theoretical development and experimental validation of the underlying PZT-structure interaction model was presented in the first part. In our newly proposed method, the damage is evaluated on the basis of the equivalent system parameters 'identified' by the surface-bonded piezo-impedance transducer. As proof of concept, the proposed method is applied to perform structural identification and damage diagnosis on a representative lab-sized aerospace structural component. It is then extended to identify and monitor a prototype reinforced concrete (RC) bridge during a destructive load test. The proposed method was found to be able to successfully identify as well as evaluate damages in both the structures.

KEYWORDS: Damage; cracks; impedance; reinforced concrete (RC); bridge.

¹**Research Scholar**, Division of Structures and Mechanics, School of Civil and Environmental Engineering, Nanyang Technological University, 50 Nanyang Avenue, Singapore 639798. **Email:** sbhalla@pmail.ntu.edu.sg.

²**Professor (Corresponding Author)**, Division of Structures and Mechanics, School of Civil and Environmental Engineering, Nanyang Technological University, 50 Nanyang Avenue, Singapore 639798. **Email:** csohck@ntu.edu.sg, **Phone:** (65) 6 790-5306, **Fax:** (65) 6 791-5093.

INTRODUCTION

The theoretical background of the electro-mechanical impedance (EMI) technique, a new NDE method, was presented in the first part of this two-part series. The first part also introduced the concept of ‘effective mechanical impedance’ and presented a new simplified electro-mechanical approach to model the interaction between the piezo-impedance transducers and their host structures in the smart systems. This paper presents the necessary analysis to extract the effective drive point (EDP) impedance of the host structure from the experimentally measured conductance and susceptance signatures. This is followed by a simplified methodology to derive structural parameters from the extracted EDP impedance and use them in identifying structural damages. Proof-of-concept applications on aerospace and civil structures are finally presented.

ANALYSIS OF COUPLED ELECTRO-MECHANICAL ADMITTANCE

As derived in the first part, the complex electro-mechanical admittance across the terminals of a square piezo-electric ceramic (PZT) patch (Length = $2l$, thickness = h), surface bonded to a structure, can be expressed as

$$\bar{Y} = G + Bj = 4\omega j \frac{l^2}{h} \left[\frac{\bar{\epsilon}_{33}^T}{(1-\nu)} - \frac{2d_{31}^2 \bar{Y}^E}{(1-\nu)} + \frac{2d_{31}^2 \bar{Y}^E}{(1-\nu)} \left(\frac{Z_{a,eff}}{Z_{s,eff} + Z_{a,eff}} \right) \bar{T} \right] \quad (1)$$

where ω is the angular frequency of excitation, $\bar{\epsilon}_{33}^T$ the complex dielectric permittivity, \bar{Y}^E the complex Young’s modulus and ν the Poisson’s ratio of the PZT patch. $Z_{a,eff}$ is the EDP impedance of the patch and $Z_{s,eff}$ that of the structure. The term \bar{T} is the complex tangent ratio, ideally equal to $(\tan \kappa l / \kappa l)$, where κ is the

complex wave number. However, in actual situations, it needs correction to accommodate the deviation of the patch from ideal behavior. Hence, \bar{T} can be expressed as

$$\bar{T} = \begin{cases} \frac{\tan(C\kappa l)}{(C\kappa l)} & \text{for single-peak behavior.} \\ \frac{1}{2} \left(\frac{\tan C_1 \kappa l}{C_1 \kappa l} + \frac{\tan C_2 \kappa l}{C_2 \kappa l} \right) & \text{for twin-peak behavior.} \end{cases} \quad (2)$$

The constants C or C_1 and C_2 , and whether the patch conforms to single-peak or twin-peak behavior can be determined from the free PZT signatures, as demonstrated in the first paper on modeling. Further, the corrected actuator effective impedance can be expressed as

$$Z_{a,eff} = \frac{2h\bar{Y}^E}{j\omega(1-\nu)\bar{T}} \quad (3)$$

By rearranging the various terms, Eq. (1) can be decomposed into two parts as

$$\bar{Y} = \underbrace{4\omega j \frac{l^2}{h} \left[\frac{\bar{\epsilon}_{33}^T}{\epsilon_{33}^T} - \frac{2d_{31}^2 \bar{Y}^E}{(1-\nu)} \right]}_{\text{Part I}} + \underbrace{\frac{8\omega d_{31}^2 l^2 \bar{Y}^E}{h(1-\nu)} \left(\frac{Z_{a,eff}}{Z_{s,eff} + Z_{a,eff}} \right) \bar{T} j}_{\text{Part II}} \quad (4)$$

It can be seen that the first part solely depends on the parameters of the PZT patch and is independent of the host structure. The structural parameters make their presence felt in part II only, in the form of the EDP structural impedance, $Z_{s,eff}$. Hence, part II alone represents the structure-PZT coupling. Thus, Eq. (4) can be written as

$$\bar{Y} = \bar{Y}_p + \bar{Y}_A \quad (5)$$

where \overline{Y}_p (part I of Eq. 4) represents the PZT contribution and \overline{Y}_A (part II of Eq. 4) represents the contribution arising from structure-PZT interaction. \overline{Y}_A is the ‘active’ component since it is sensitive to any changes in the structure (any change in $Z_{s,eff}$, say due to damage) in the vicinity of the patch. \overline{Y}_p , on the contrary, is a ‘passive’ component, since it is insensitive to any structural damage. \overline{Y}_p can be broken down into real and imaginary parts by expanding $\overline{\epsilon}_{33}^T = \epsilon_{33}^T(1 - \delta j)$ and $\overline{Y}_{33}^E = Y_{33}^E(1 + \eta j)$ and can be expressed as

$$\overline{Y}_p = G_p + B_p j \quad (6)$$

$$\text{where } G_p = \frac{4\omega l^2}{h} \left\{ \delta \epsilon_{33}^T + \frac{2d_{31}^2 Y_{11}^E \eta}{(1 - \nu)} \right\} \quad \text{and} \quad B_p = \frac{4\omega l^2}{h} \left\{ \epsilon_{33}^T - \frac{2d_{31}^2 Y_{11}^E}{(1 - \nu)} \right\} \quad (7)$$

Typically, B_p is characterized by a large magnitude (comparable to B) whereas G_p displays a small magnitude, due to the presence of the small order terms η and δ (η and δ respectively denote mechanical loss factor and dielectric loss factor of the PZT patch). In the measured susceptance signature, usually B_p camouflages the active component, which is why the raw-susceptance signature is not very popular for structural health monitoring. However, we can accurately predict G_p and B_p if we record the conductance and the susceptance signatures of PZT patches in the ‘free-free’ condition, prior to their bonding to the host structures, as demonstrated in the first paper on modeling. Hence, the PZT contribution can be filtered off and active admittance derived as : $\overline{Y}_A = \overline{Y} - \overline{Y}_p$. Thus, the active components (G_A and B_A) can be derived from the measured raw admittance signatures (G and B) as

$$G_A = G - G_p \quad \text{and} \quad B_A = B - B_p \quad (8)$$

In complex form, we can express the active component as

$$\overline{Y}_A = G_A + B_A j = \frac{8\omega d_{31}^2 \overline{Y}_1^E l^2}{h(1-\nu)} \left(\frac{Z_{a,eff}}{Z_{s,eff} + Z_{a,eff}} \right) \overline{T} j \quad (9)$$

It was demonstrated by the authors (Bhalla et al. 2002; Bhalla and Soh 2003), for 1D case, that the elimination of the passive component renders the admittance signatures more sensitive to any structural damages. Besides, this process also enables the utilization of the imaginary component (so far deemed redundant), in damage identification. The same holds true for the 2D PZT-structure interaction considered in this paper. Therefore, it is more pragmatic to utilize the active component rather than the raw signatures for non-destructive evaluation (NDE) and structural health monitoring (SHM).

EXTRACTION OF STRUCTURAL MECHANICAL IMPEDANCE

Bhalla and Soh (2003) outlined a computational procedure for extracting 1D drive point mechanical impedance of skeletal structures from the active admittance signatures of surface-bonded piezo-impedance transducers. The computational procedure described in this section is not only more concise but at the same time applicable to all structure types since it is based on effective impedance model formulated in the first paper on modeling. Substituting $\overline{Y}^E = Y^E(1 + \eta j)$ and $\overline{T} = r + tj$ into Eq. (9) and rearranging the various terms, we obtain

$$M + Nj = \left(\frac{Z_{a,eff}}{Z_{s,eff} + Z_{a,eff}} \right) (R + Sj) \quad (10)$$

where

$$M = \frac{B_A h(1-\nu)}{8\omega l^2 d_{31}^2 Y^E} \quad \text{and} \quad N = -\frac{G_A h(1-\nu)}{8\omega l^2 d_{31}^2 Y^E} \quad (11)$$

$$R = r - \eta t \quad \text{and} \quad S = t + \eta r \quad (12)$$

Further, expanding $Z_{S,eff} = x + yj$ and $Z_{a,eff} = x_a + y_a j$, and upon solving, we can obtain the components of the EDP structural impedance as

$$x = \frac{M(x_a R - y_a S) + N(x_a S + y_a R)}{M^2 + N^2} - x_a \quad (13)$$

$$y = \frac{M(x_a S + y_a R) - N(x_a R - y_a S)}{M^2 + N^2} - y_a \quad (14)$$

In these computations, the term \bar{T} , which depends upon $\tan \kappa l / \kappa l$ (see Eq. 2), plays a significant role. Liang et al. (1994) approximated $(\tan \kappa l / \kappa l)$ as unity, assuming the operational frequency to be very small as compared to the resonating frequency of the PZT patch. However, in SHM applications, this is usually not the case since the operational frequencies (few kHz to few hundreds of kHz) are of the order of the natural frequencies of the patch. Therefore, it is essential to determine this quantity precisely. Denoting κl by z , we can write

$$\frac{\tan \kappa l}{\kappa l} = \frac{\sin z}{z \cos z} \quad (15)$$

Noting from the theory of complex numbers (Kreyszig 1993) that

$$\cos z = \frac{e^{iz} + e^{-iz}}{2} \quad \text{and} \quad \sin z = \frac{e^{iz} - e^{-iz}}{2i}, \quad (16)$$

and substituting $z = rl + (im)j$, we obtain after solving

$$\frac{\tan \kappa l}{\kappa l} = \left(\frac{au - bv}{u^2 + v^2} \right) - \left(\frac{av + bu}{u^2 + v^2} \right) j \quad (17)$$

where

$$a = [e^{-im} + e^{im}] \sin(rl) \quad \text{and} \quad b = [e^{-im} - e^{im}] \cos(rl) \quad (18)$$

$$c = [e^{-im} + e^{im}] \cos(rl) \quad \text{and} \quad d = [e^{-im} - e^{im}] \sin(rl) \quad (19)$$

$$u = c(rl) - d(im) \quad \text{and} \quad v = d(rl) + c(im) \quad (20)$$

The computational procedure outlined here facilitates the determination of the EDP impedance of the structure, $Z_{s,eff} = x + yj$, at a particular frequency ω , from the active admittance signatures. Following this procedure, ‘x’ and ‘y’ can be determined for the entire frequency range of interest. This procedure was employed to extract the structural EDP impedance of the test structure used for validating the new impedance model in the first paper on modeling (aluminum block 48x48x10mm in size). Fig. 1 shows a plot of $|Z_{eff}|^{-1}$, worked out by this procedure, comparing it with the inverse EDP impedance predicted by finite element method (details covered in the first paper). Reasonably good agreement can be observed between the two. The main reason for plotting $|Z_{s,eff}|^{-1}$ (instead of $Z_{s,eff}$) is that the resonant frequencies can be easily identified as peaks of the plot. It was previously demonstrated by the authors (Bhalla and Soh 2003) that the utilization of ‘x’ and ‘y’ rather than raw signatures leads not only to higher damage sensitivity but also provides greater insight into the mechanism associated with structural damage. Therefore, we present in the next section a generalized procedure to derive system parameters from the structural EDP impedance.

SYSTEM PARAMETER IDENTIFICATION

The structural EDP impedance, extracted by means of the procedure outlined above, carries information about the dynamic characteristics of the host structure. Bhalla and Soh (2003) idealized the host structure (1D skeletal structure) as a parallel combination of a resistive element (damper) and a reactive element (stiffness-mass factor). This section presents a more general approach to predict the equivalent structural system much more accurately. Before analyzing any

complicated structural system, it would be a worthwhile exercise to study the impedance behavior of some simple systems. Fig. 2 shows the plots of the real and the imaginary components of the mechanical impedance of basic structural elements- the mass, the spring and the damper. These basic elements can be combined in a number of ways to develop complex mechanical systems. Table 1 shows the impedance plots for some simple series and parallel connections of the basic elements (Hixon 1988). The two components of the extracted EDP impedance may not display an ideal behavior, such as pure mass or pure stiffness or pure damper. Rather, they might display an impedance spectra similar to a combination of the basic elements. Both the resistive and the reactive terms might vary with frequency. The ‘unknown’ structure can thus be idealized as a simple structure (series or parallel combination of basic elements), and the equivalent system parameters can therefore be determined.

To demonstrate this approach, let us employ the PZT patch S2002-6 (10x10x0.3mm in size), whose updated model was obtained in the first paper on modeling. This patch was surface bonded to an aluminum block, 50x48x10mm in size (grade Al 6061 T6), representing an unknown structural system. The raw signatures were processed so as to filter off the passive component and to extract the structural EDP impedance. A close examination of the extracted impedance components in the frequency range 25-40 kHz suggested that the system behavior was similar to a parallel spring-damper (k-c) combination (system 1 in Table 1). The system parameters were worked out as $c = 36.54 \text{ Ns/m}$ and $k = 5.18 \times 10^7 \text{ N/m}$. The analytical plots of ‘x’ and ‘y’ obtained by these equivalent parameters match well with their experimental counterparts, as shown in Fig. 3.

Similarly, in the frequency range 180-200kHz, the system behavior was found to be similar to a parallel spring-damper (k-c) combination in series with mass m (system 11 in Table 1). A set of system parameters $c = 1.1 \times 10^{-3}$ Ns/m, $k = 4.33 \times 10^5$ N/m and $m = 3.05 \times 10^{-7}$ kg produced similar system behavior, as shown in Fig. 4. Further refinement was achieved by adding a spring $K^* = 7.45 \times 10^7$ N/m and a damper $C^* = 12.4$ Ns/m in parallel, to make the equivalent system appear as shown in Fig. 5. Fig. 6 shows the comparison between the experimental plots with the analytical plots for this equivalent system. Extremely good agreement can be observed between the plots obtained experimentally and those pertaining to the equivalent system. Hence, the structural system is 'identified' with a reasonably good accuracy.

Thus, this procedure enables us to 'identify' any unknown structure without demanding any a-priori information governing the phenomenological nature of the structure. The only requirement is an 'updated' model of the PZT patch, which can be derived from preliminary specifications of the PZT patch and its admittance signatures in the 'free-free' conditions, as demonstrated in the first part.

DAMAGE DIAGNOSIS IN AEROSPACE AND MECHANICAL SYSTEMS

This section describes a damage detection study carried out on the aluminum block, 50x48x10mm in size, identified using a surface bonded PZT patch in the previous section. This is a typical small-sized rigid structure characterized by very high natural frequencies. Many critical aircraft components such as turbo engine blades are small and rigid, and are characterized by typically

high natural frequencies in the kHz range (Giurgiutiu and Zagrai 2002), and hence exhibit similar dynamic behavior.

Damage was induced in this test structure by drilling holes, 5mm in diameter, through the thickness of the specimen. Three different levels of damage were induced- incipient, moderate and severe, as shown in Fig. 7. The number of holes was increased from two to eight in three stages to simulate a gradual growth of damage from incipient type to severe type. After each damage, the admittance signatures of the PZT patches were recorded and the equivalent structural parameters were worked out. Fig. 8 shows the effect of these damages on the real and the imaginary components of mechanical impedance in the frequency range 25-40 kHz. Fig. 9 shows the effect of damages on the identified structural parameters. As expected, the identified stiffness can be observed to reduce and the damping increase with damage progression. The stiffness was found to reduce by about 12% and the damping increase by about 8% after the incipient damage. After that, with damage propagation, very small further drop/ increase was observed. However, the incipient damage was identified very clearly.

Fig. 10 shows the effect of these damages on the impedance spectra in the frequency range of 180-200 kHz. Equivalent lumped system parameters were similarly determined for each damage state. Fig. 11 shows a comparison between the experimental impedance plots and the plots based on the equivalent system parameters for each damage state. The effect of these damages on the extracted equivalent parameters is shown in Fig. 12. With damage progression, mass and stiffness can be seen to reduce and the damping can be observed to increase. The stiffness was found to reduce gradually- 17% for the incipient damage, 31% for the

moderate damage and 47% for the severe damage. Mass was also found to similarly reduce with damage severity- 16% for the incipient damage, 28% for the moderate damage and 42% for the severe damage. The damping values (c and C^*) were also found to similarly increase (Figs. 12c and 12e), though ' c ' displayed a slight decrease after the incipient damage. The only exception is observed in the parallel stiffness K^* , which remains more or less unaffected by damage. Contrary to the 25-40kHz range, the 180-200kHz range can diagnose the damages much better, since significant variation is observed for moderate and severe damages as well. Fig. 13 shows plot between the area of the specimen (a measure of the residual capacity of the specimen) and the equivalent ' k ' identified by the PZT patch. Following empirical relation was worked out between the two by regression analysis

$$A = 1874.2 + 0.0021k - 2.02 \times 10^{-9} k^2 \quad (21)$$

In this manner, we can calibrate the damage sensitive system parameters with damage and can use them for damage diagnosis in real scenarios.

The observed sensitivity of damage detection is much higher in the frequency range 180-200kHz. This is due to the fact that with increase in frequency, the wavelength of the induced stress wave gets smaller and is therefore more sensitive to any defects and damages. This is also due to the presence of a damage sensitive vibrational mode in the frequency range 180-200kHz (Fig. 10) and its absence in the 25-40kHz range (Fig. 8). This agrees with the recommendation of Sun et al. (1995), that the frequency range must contain prominent vibrational modes. However, it should be noted that in spite of the absence of any major resonance mode in the frequency range 25-40 kHz, the incipient damage is still identified reasonably well, although damage severity is not quantified well.

Hence, the proposed method can evaluate structural damages in aerospace components reasonably well. Besides, the methodology is also ideal for identifying damages in precision machinery components, turbo machine parts and computer parts such as the hard disks. These components are quite rigid and exhibit a dynamic behavior similar to the test structure described in this section.

EXTENSION TO DIAGNOSIS OF CIVIL-STRUCTURAL SYSTEMS

In order to test the feasibility of the proposed methodology for monitoring large civil-structures, the data recorded during the destructive load test on a prototype reinforced concrete (RC) bridge (Soh et al. 2000) was utilized. The test bridge consisted of two spans of about 5m, instrumented with several PZT patches, 10x10x0.2mm in size, manufactured by PI Ceramic (2003). Key mechanical and electrical properties of the PZT patch are listed in Table 2. The bridge was subjected to three load cycles so as to induce progressively severe damages. Details of the instrumentation as well as loading can be found in reference (Soh et al. 2000). Root mean square deviation (RMSD) index was used to evaluate damages in the previous study. In the present investigation, the evaluation of damage is carried out more realistically using the newly developed approach.

Fig. 14 shows a view of the top surface of the deck after cycle II. Eight patches, marked 1 through 8 were installed on the bridge surface. These patches detected the presence of surface cracks much earlier than other sensors such as the strain gauges (Soh et al. 2000). We typically selected patch 4 as a representative PZT in the present analysis. Fig. 15 shows the impedance spectra of the pristine structure identified by the PZT patch 4 in the frequency range 120-140 kHz. The

patch ‘identified’ the structure as a parallel spring-damper combination, the identified parameters being $k = 9.76 \times 10^7$ N/m and $c = 26.1823$ Ns/m. The equivalent parameters were also determined for the damaged bridge, after cycles I and II. Fig. 16 provides a look at the associated damage mechanism- k reducing and c increasing with damage progression. Reduction in the stiffness and increase in the damping are well-known phenomenon associated with crack development in concrete (Esteban 1996). Damping increased by about 20% after cycle I and about 33% after cycle II. This correlated well with the appearance of cracks in the vicinity of this patch. Stiffness was found to reduce marginally by about 3% only, after cycle II, indicating the higher sensitivity of damping to damage as compared to stiffness. The same phenomenon was also observed during tests on RC frame (Bhalla and Soh 2003). More rigorous analysis will be presented in subsequent publications.

Thus, the proposed methodology can be easily extended to large civil-structures. However, it should be noted that owing to the large structure, the patch can only ‘identify’ the localized portion of the structure, typically representative of the zone of influence. For such large structures, complete monitoring demands an array of PZT patches, which can be monitored on one-by-one basis and can thus localize as well as evaluate the extent of damages.

DISCUSSIONS

The newly proposed methodology of identifying a structure and evaluating damages from the identified parameters has wide range of applications from aerospace components to large civil-structures. In order to make greater utilization

of the proposed methodology, we need to calibrate the identified system parameters with damage progression. Presently, we have found an empirical relationship between the residual capacity of the specimen and the equivalent stiffness as identified by the PZT, for the representative aerospace structural component.

The main advantages of the piezo-impedance transducers as compared to other sensor systems are their low-cost, easy installation, high damage sensitivity, noise immunity and good dynamic behavior (Park et al. 2000; Bhalla and Soh 2003). Being small in size and stiffness, they are not expected to alter the dynamic properties of the test structure itself. This is especially important for miniaturized precision machine parts (Giurgiutiu and Zagari 2002). Easy installation makes these transducers much more favorable than any other sensor type for civil-structures. Since they are surface bonded (contrary to some sensors which call for implantation inside the concrete), they stand equally useful for already-built structures as they will be for the to-be-built structures. Besides, commercially available impedance analyzer is used for acquiring the admittance signatures from the piezo-transducers . Currently, low-cost and portable versions of impedance analyzer are under development (Peairs et al. 2003), which will make the technique even more economical in the near future.

CONCLUSIONS

This paper has presented a new simplified diagnostic approach for identification and NDE of structures based on the equivalent system 'identified' by means of the EMI technique. It makes use of real as well as imaginary components of the admittance signature for determining damage sensitive equivalent structural

parameters. As proof of concept, the method has been successfully applied to diagnose damages on a representative aerospace structure and a prototype civil structure. The piezo-impedance transducers can be installed on the inaccessible parts of crucial machine components, aircraft main landing gear fitting or turbo-engine blades and civil-structures to perform continuous real-time SHM. Key advantage of the proposed method lies in the fact that the equivalent system is identified from the experimental data alone. The approach is not only simple to use but at the same time provides an essence of the associated damage mechanism.

APPENDIX I. REFERENCES

- Bhalla S., Naidu A. S. K., Soh C. K (2002). "Influence of Structure-Actuator Interactions and Temperature on Piezoelectric Mechatronic Signatures for NDE", *Proc. ISSS-SPIE Conference on Smart Materials, Structures and Systems*, Bangalore, Dec. 12-14, 2002; 213-219.
- Bhalla, S., and Soh, C. K. (2003). "Structural Impedance Based Damage Diagnosis by Piezo-Transducers", *Earthquake Engineering and Structural Dynamics*, 32(12), 1897-1916.
- Esteban, J. (1996). "Analysis of the Sensing Region of a PZT Actuator-Sensor", *Ph.D. Dissertation*, Virginia Polytechnic Institute and State University, Blacksburg, VA.
- Giurgiutiu, V., and Zagrai, A. N. (2002). "Embedded Self-Sensing Piezoelectric Active Sensors for On-Line Structural Identification", *Journal of Vibration and Acoustics*, ASME, 124(1), 116-125.
- Hixon, E.L. (1988). "Mechanical Impedance", *Shock Vibration Handbook*, C. M. Harris, editor, 3rd ed., Mc Graw Hill Book Co., New York, 10.1-10.46.
- Kreyszig E. (1993). *Advanced Engineering Mathematics*, 7th edn., Wiley, New York.
- Liang, C., Sun, F. P., and Rogers, C. A. (1994). "Coupled Electro-Mechanical Analysis of Adaptive Material Systems- Determination of the Actuator Power Consumption and System Energy Transfer", *Journal of Intelligent Material Systems and Structures*, 5(1), 12-20.

- Park, G., Cudney, H. H. and Inman, D. J. (2000), “Impedance-Based Health Monitoring of Civil Structural Components”, *Journal of Infrastructure Systems*, ASCE, 6(4), 153-160.
- Peairs, D. M., Park, G., and Inman, D. J. (2003). “Improving Accessibility of the Impedance-Based Structural Health Monitoring Method”, *Journal of Intelligent Material Systems and Structures*, in press.
- PI Ceramic (2003). Product Catalogue, Lindenstrabe, Germany, <http://www.piceramic.de>, (20 January, 2003).
- Soh, C. K., Tseng, K. K.-H., Bhalla, S., and Gupta, A. (2000). “Performance of Smart Piezoceramic Patches in Health Monitoring of a RC Bridge”, *Smart Materials and Structures*, 9(4), 533-542.
- Sun, F. P., Chaudhry, Z., Rogers, C. A., Majmundar, M., and Liang, C. (1995). “Automated Real-Time Structure Health Monitoring via Signature Pattern Recognition”, *Proc., SPIE Conference on Smart Structures and Materials Conference*, San Diego, California, Feb.27-Mar1, 2443, 236-247.

APPENDIX II. NOTATION

A	=	Area;
B	=	Susceptance;
C	=	Correction factor to update model of PZT;
c	=	Damping constant;
d	=	Piezoelectric strain coefficient;
G	=	Conductance;
h	=	Thickness of PZT patch;
j	=	$\sqrt{-1}$;

k, K	=	Spring constant;
l	=	Half-length of PZT patch;
S	=	Mechanical strain;
\bar{T}	=	Complex tangent function;
V	=	Electric voltage;
\bar{Y}	=	Complex electro-mechanical admittance;
$\overline{Y^E}$	=	Complex Young's modulus of elasticity at constant electric field;
Z	=	Mechanical impedance;
$\overline{\varepsilon^T}$	=	Complex electric permittivity at constant stress;
ω	=	Angular velocity;
ν	=	Poisson's ratio;
κ	=	Wave number;
η	=	Mechanical loss factor;
δ	=	Electrical loss tangent;
x, y	=	Real and imaginary components of mechanical impedance;

Subscripts

A	=	Active;
P	=	Passive;

Superscripts

T	=	Quantity at constant stress;
E	=	Quantity at constant electric field;

LIST OF FIGURES AND TABLES

(AS/2003/022179)

Fig. 1 Comparison between $|Z_{\text{eff}}|^{-1}$ obtained experimentally and numerically.

Fig. 2 Real and imaginary components of mechanical impedance of basic elements. (a) Real part. (b) Imaginary part.

Fig. 3 Mechanical impedance in 25-40kHz frequency range.

(a) Real part. (b) Imaginary part.

Fig. 4 Mechanical impedance in 180-200 kHz frequency range.

(a) Real part. (b) Imaginary part.

Fig. 5 Refinement of equivalent system by the introduction of an additional spring K^* and additional damper C^* .

Fig. 6 Mechanical impedance in 180-200kHz frequency range. The equivalent system plots are obtained for the system shown in Fig.6.

(a) Real part. (b) Imaginary part.

Fig. 7 Various levels of damage induced on test specimen.

Fig. 8 Effect of damage on extracted mechanical impedance in 25-40kHz range.

(a) Real part. (b) Imaginary part.

Fig. 9 Effect of damage on equivalent system parameters.

(a) Equivalent damping constant. (b) Equivalent spring constant.

Fig. 10 Effect of damage on extracted mechanical impedance of test structure in 180-200kHz range. (a) Real part. (b) Imaginary part.

Fig. 11 Determination of equivalent system parameters for various damage states.

(a) Incipient damage: Real part. (b) Incipient damage: Imaginary part.

- (c) Moderate damage: Real part. (d) Moderate damage: Imaginary part.
(d) Severe damage: Real part. (f) Severe damage: Imaginary part.

Fig. 12 Effect of damage on equivalent system parameters.

- (a) Equivalent spring constant. (b) Equivalent mass.
(b) Equivalent damping constant. (d) Equivalent additional spring constant.
(e) Equivalent additional damper.

Fig. 13 Plot of residual specimen area versus equivalent spring constant.

Fig. 14 Damage diagnosis of a prototype RC bridge using proposed methodology.

Fig. 15 Mechanical impedance of RC bridge in 120-140kHz frequency range. The equivalent system plots are obtained for a parallel spring damper combination.

- (a) Real part. (b) Imaginary part.

Fig. 16 Effect of damage on equivalent system parameters of RC bridge.

- (a) Equivalent damping. (b) Equivalent spring constant.

Table 1 Mechanical impedance of combinations of spring, mass and damper.

Table 2 Key properties of PZT patch (PI ceramic, 2003)

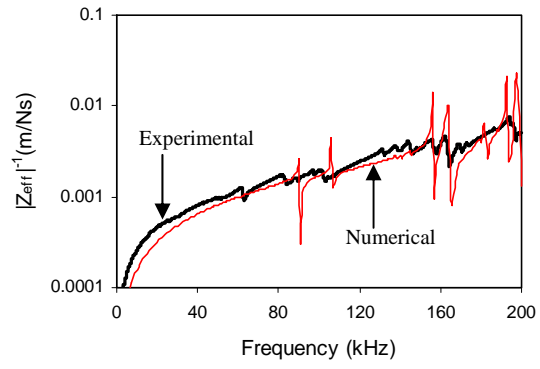
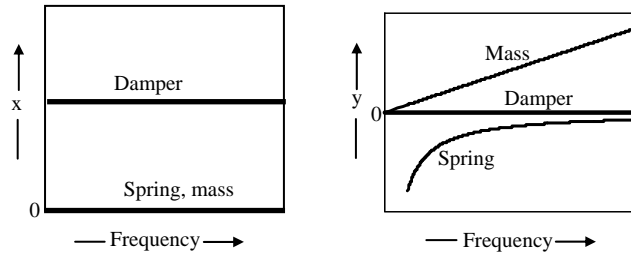


Fig. 1 Comparison between $|Z_{\text{eff}}|^{-1}$ obtained experimentally and numerically.



(a)

(b)

Fig. 2 Real and imaginary components of mechanical impedance of basic elements. (a) Real part. (b) Imaginary part.

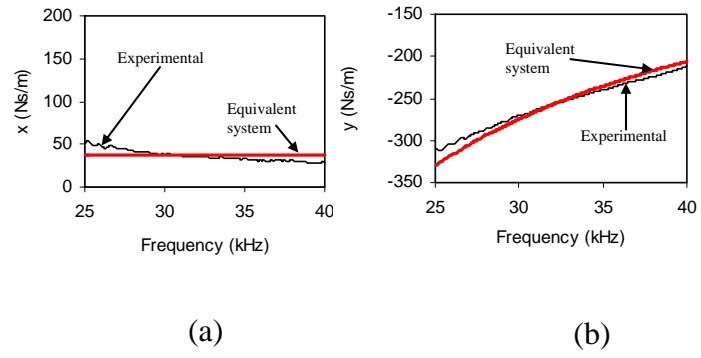


Fig. 3 Mechanical impedance in 25-40kHz frequency range.

(a) Real part. (b) Imaginary part.

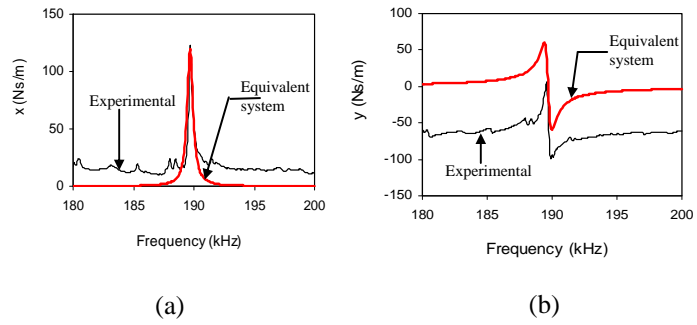


Fig. 4 Mechanical impedance in 180-200 kHz frequency range.

(a) Real part. (b) Imaginary part.

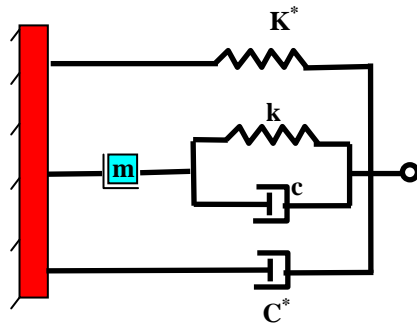
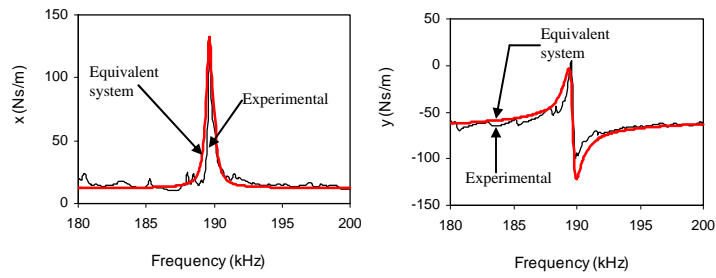


Fig. 5 Refinement of equivalent system by the introduction of an additional spring K^* and additional damper C^* .



(a)

(b)

Fig. 6 Mechanical impedance in 180-200kHz frequency range. The equivalent system plots are obtained for the system shown in Fig. 5.

(a) Real part.

(b) Imaginary part.

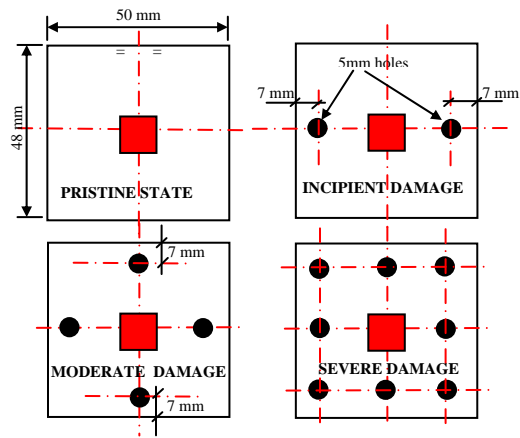
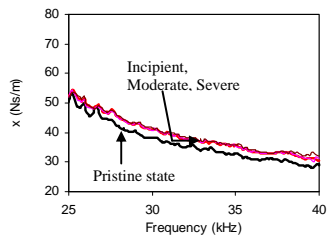
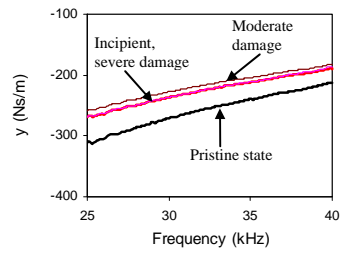


Fig. 7 Various levels of damages induced on test specimen.



(a)



(b)

Fig. 8 Effect of damage on extracted mechanical impedance in 25-40kHz range.

(a) Real part. (b) Imaginary part.

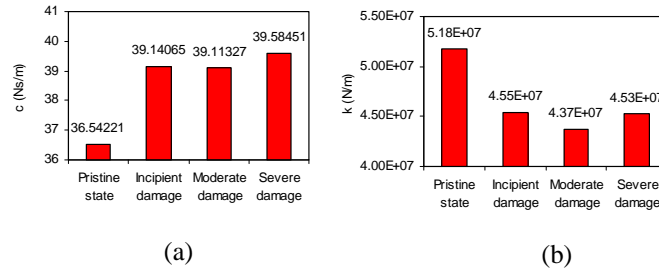


Fig. 9 Effect of damage on equivalent system parameters.

(a) Equivalent damping constant. (b) Equivalent spring constant.

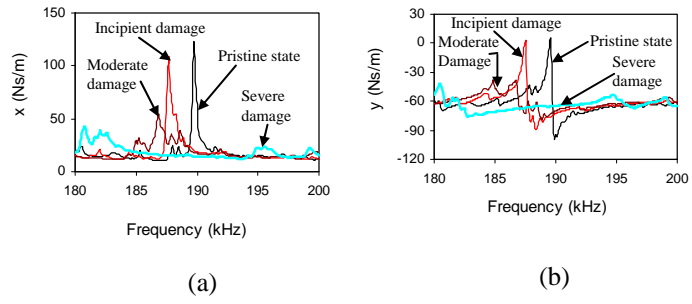


Fig. 10 Effect of damage on extracted mechanical impedance of test structure in 180-200kHz range. (a) Real part. (b) Imaginary part.

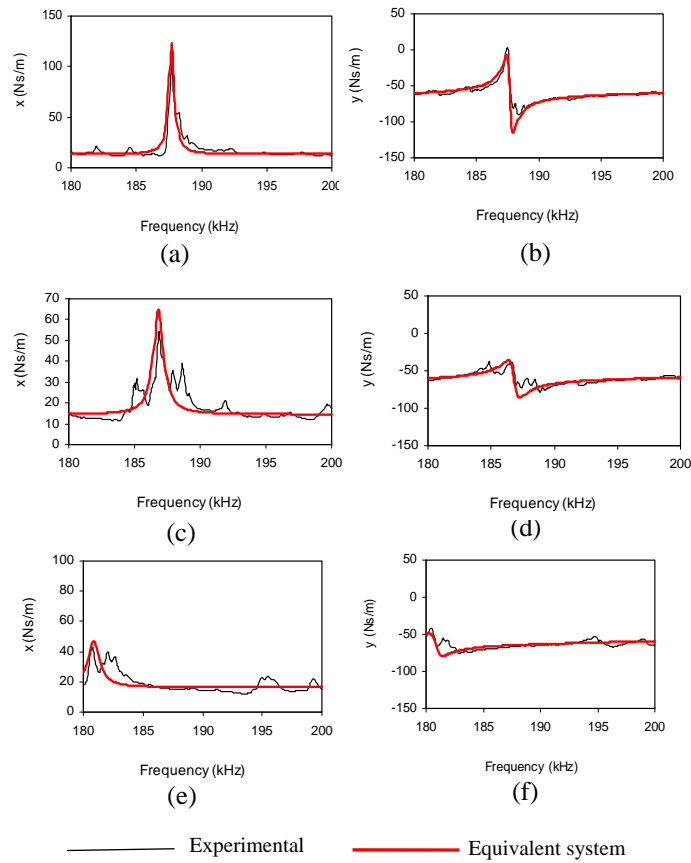


Fig. 11 Determination of equivalent system parameters for various damage states.

- (a) Incipient damage: Real part. (b) Incipient damage: Imaginary part.
(c) Moderate damage: Real part. (d) Moderate damage: Imaginary part.
(e) Severe damage: Real part. (f) Severe damage: Imaginary part.

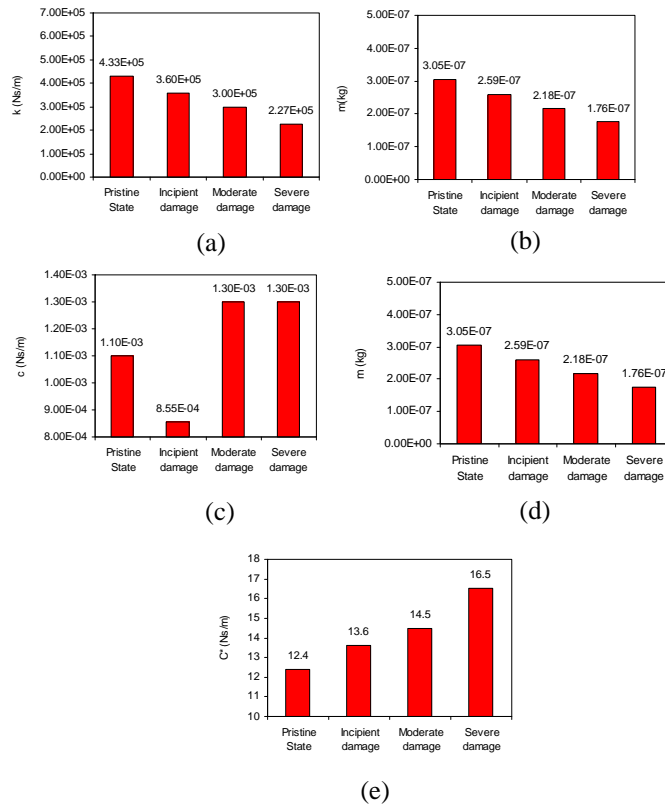


Fig. 12 Effect of damage on equivalent system parameters.

(a) Equivalent spring constant. (b) Equivalent mass. (c) Equivalent damping constant.

(d) Equivalent additional spring constant. (e) Equivalent additional damper.

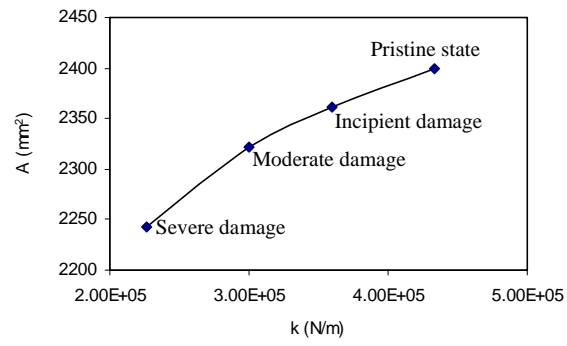


Fig. 13 Plot of residual specimen area versus equivalent spring constant.

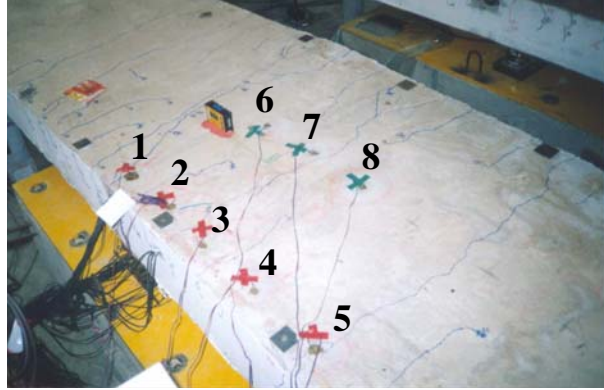


Fig. 14 Damage diagnosis of a prototype RC bridge using proposed methodology.

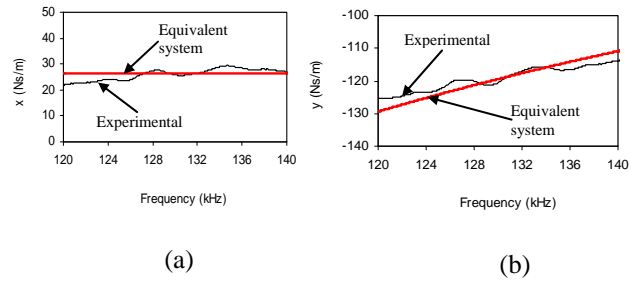


Fig. 15 Mechanical impedance of RC bridge in 120-140kHz frequency range. The equivalent system plots are obtained for a parallel spring damper combination.

(a) Real part. (b) Imaginary part.

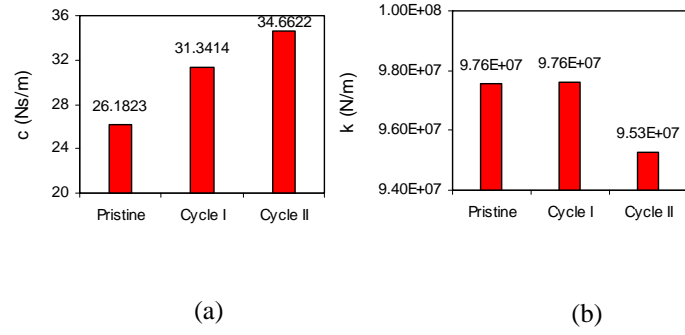

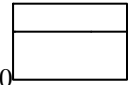
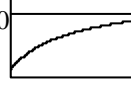
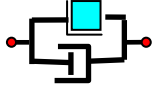
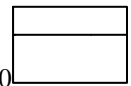
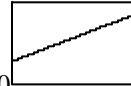

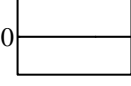
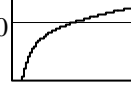
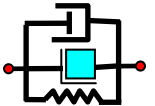
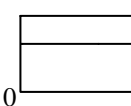
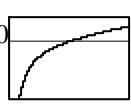
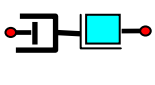

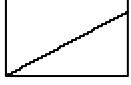
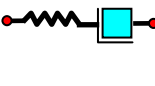
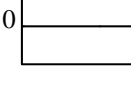
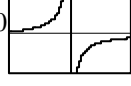
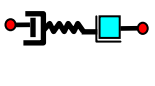

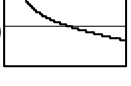
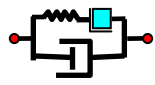
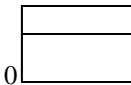
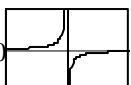
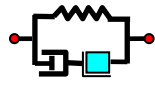


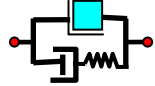
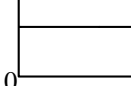
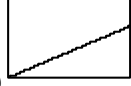
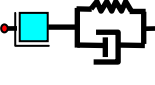
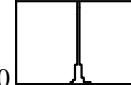
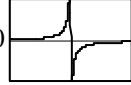
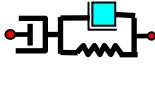


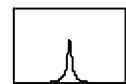


Fig. 16 Effect of damage on equivalent system parameters of RC bridge.

(a) Equivalent damping. (b) Equivalent spring constant.

Table 1 Mechanical impedance of combinations of spring, mass and damper.

No. (1)	COMBIN— ATION (2)	x (3)	y (4)	x vs Freq. (5)	y vs Freq. (6)
1		c	$-\frac{k}{\omega}$		
2		c	$m\omega$		
3		0	$m\omega - \frac{k}{\omega}$		
4		c	$m\omega - \frac{k}{\omega}$		
5		$\frac{c^{-1}}{c^{-2} + (\omega m)^{-2}}$	$\frac{(\omega m)^{-1}}{c^{-2} + (\omega m)^{-2}}$		
6		0	$\frac{-1}{(\omega/k) - (\omega m)^{-1}}$		
7		$\frac{c^{-1}}{c^{-2} + (\omega/k - 1/\omega m)^2}$	$\frac{-(\omega/k - 1/\omega m)}{c^{-2} + (\omega/k - 1/\omega m)^2}$		
8		c	$\frac{\omega m k}{k - \omega^2 m}$		
9		$\frac{c^{-1}}{c^{-2} + (\omega m)^{-2}}$	$\frac{m^{-1} - k(c^{-2} + \omega^{-2} m^{-2})}{\omega [c^{-2} + (\omega m)^{-2}]}$		
10		$\frac{c^{-1}}{c^{-2} + (\omega/k)^2}$	$\frac{\omega [m(c^{-2} + \omega^2 k^{-2}) - k^{-1}]}{c^{-2} + (\omega/k)^2}$		
11		$\frac{cm^2\omega^2}{c^2 + (\omega m - k/\omega)^2}$	$\frac{m\omega [c^2 - \frac{k}{\omega}(\omega m - k/\omega)]}{c^2 + (\omega m - k/\omega)^2}$		
12		$\frac{c^{-1}}{c^{-2} + [\omega/(k - m\omega^2)]^2}$	$\frac{-\omega/(k - m\omega^2)}{c^{-2} + [\omega/(k - m\omega^2)]^2}$		



0



13		$\frac{ck^2 / \omega^2}{c^2 + (\omega m - k / \omega)^2}$	$\frac{-km \left[(\omega m - k / \omega) + \frac{c^2 k}{\omega m} \right]}{c^2 + (\omega m - k / \omega)^2}$	0	
----	---	---	---	---	---

Table 2 Key properties of PZT patch (PI Ceramic, 2003).

Physical Parameter (1)	Value (2)
Density (kg/m ³)	7800
Electric Permittivity, ϵ_{33}^T (farad/m)	2.124×10^{-8}
Piezoelectric Strain Coefficient, d_{31} (m/V)	-2.10×10^{-10}
Young's Modulus, Y_{11}^E (N/m ²)	6.667×10^{10}
Dielectric loss factor, $\tan \delta$	0.015